ISUAAAT15-084

ESTIMATION OF UNSTEADY BLADE LOADING DUE TO INLET DISTORTION USING A BODY FORCE ROTOR MODEL

J. J. Defoe

Turbomachinery and Unsteady Flows
Research Group
Department of Mechanical,
Automotive, and Materials Engineering
University of Windsor
Windsor, ON N9B 3P4, Canada
Email: jdefoe@uwindsor.ca

Q. J. Minaker

Turbomachinery and Unsteady Flows
Research Group
Department of Mechanical,
Automotive, and Materials Engineering
University of Windsor
Windsor, ON N9B 3P4, Canada

W. J. Altenhof

Department of Mechanical, Automotive, and Materials Engineering
University of Windsor
Windsor, ON N9B 3P4, Canada

ABSTRACT

In this paper an approach for estimating unsteady rotor blade loading due to inlet distortion in turbomachines is introduced and demonstrated. A body force representation of the turbomachinery in a full-annulus flow field computation yields the spatially-varying pressure field and forces in the rotor swept volume. The body force model does not require specification of the blade thickness. After definition of a thickness distribution, the computed pressure and force fields are used to estimate the time-varying surface pressures acting on a rotor blade over the course of one revolution. A finite element computation in which this surface pressure loading is applied gives the time-varying stresses. Single-passage flow computations including the blade shape details yield aerodynamic performance predictions. An example case study is included for a low-speed axial fan. It is found that several inlet distortions all yield the same region of highest time-varying blade stress: the leading edge near the hub. Comparing initial and thickened blades, a trade-off is quantified as follows: thickening the blade in the region of highest time-varying stress by at most 4% of chord reduces stage efficiency by 2.4% but lowers the peak time-varying stress by a factor of 3.6.

NOMENCLATURE

$A =$ area
$B =$ number of blades in a blade row
$b =$ blade passage open area fraction
$c =$ blade chord
$d =$ deviation
$F =$ force per unit volume
$f =$ frequency
$h =$ enthalpy
$k =$ number of body force grid points in circumferential direction
$\dot{m} =$ mass flow rate
$\hat{n} =$ normal
$p =$ pressure
$q =$ local blade thickness
$R =$ radius
$\mathscr{R} =$ specific gas constant
$r =$ radial coordinate
$s =$ entropy

Copyright © 2018 by ISUAAAT Scientific Committee

t = time
U = blade speed = Ωr
V = velocity in stationary reference frame
W = velocity in rotor reference frame
x = axial coordinate
δ = boundary layer thickness for vertically stratified distortion
ϕ = flow coefficient
θ = circumferential coordinate
ψ = work coefficient
ρ = density
σ = stress
Ω = rotor angular velocity
ω = entropy-based loss coefficient

SUBSCRIPTS

0 = quantity at initial time
0% = quantity at the hub
25% = quantity at 25% span
bf = body force related
blade = blade related
c = camber surface
des = design value
in = inflow boundary value
LE = leading edge
max = maximum
mid = 50% span value
PS = pressure side
q = thickness
RMS = root mean squared
red = reduced
rf = relative flow
rot = rotor
SS = suction side
t = stagnation quantity
vm = von Mises
x = axial component
y = yield
θ = tangential component

SUPERSCRIPTS

M = mass-weighted average quantity
$\prime$ = quantity defined relative to propeller axis

INTRODUCTION

Aeromechanical forced response prediction via computational fluid dynamics (CFD) is a well-studied field. A few salient examples are discussed here but no attempt is made at an exhaustive review. He [1] provides a useful overview of the field, highlighting several important characteristics of past work. Many of the approaches for reducing the computational cost of predicting the unsteady loading require specialized solvers and/or complicated boundary conditions. As a result these approaches, while accurate and effective, are not highly accessible to a typical CFD user. In addition, they generally require the full details of the blade geometry for the rotor(s) and stator(s) of interest. This may not be available at the preliminary design stage. Hall et al.'s harmonic balance method [2] is able to provide accurate assessment of unsteady aerodynamic forcing at relatively low computational cost. The disadvantage of this method is the complexity of its implementation. It also requires the full blade geometry details to be known as the blades are included in the numerical simulations. Rahmati et al. [3] developed an innovative computational approach that can capture the effects of interactions between blade rows on aeromechanical loading. While effective and efficient, the approach requires use of a custom solver and thus is not broadly accessible. It also requires a complete description of the blade geometry as input to the flow simulations.

Unsteady loading on blades caused by inlet flow distortion has been considered in the past, for example by Manwaring et al. [4]. The authors experimentally measured and numerically predicted the vibratory blade response caused by inlet flow distortion. In the numerical approach taken, the full blade geometry needed to be defined before the loading on the blades could be determined.

The problem remains that existing methods provide no inexpensive way of estimating the unsteady loading on a rotor caused by inlet distortion without custom solvers, significant modification of existing solvers, or expensive full-annulus unsteady CFD. In addition the detailed three-dimensional blade geometry is typically required a priori.

In this paper, we propose the use of a flow field obtained using a body force representation of the turbomachinery as the basis for estimating the unsteady blade loading. Body force models have been used to predict steady and unsteady aerodynamics by replacing the blade row swept volume with distributed source terms of (in general) mass, momentum, and energy [5–7]. One advantage of using a body force model of the blade rows is that it is easy to implement. No special solvers or boundary conditions are required, and nearly all modern CFD codes support the addition of user-defined source terms to the governing equations. These computations can typically be carried out on relatively coarse grids and only steady solutions are required even in non-uniform inflow [8, 9]. From the pressure field within the rotor swept volume and the body force source terms computed, it is possible to estimate the variations in loading on the blades as they rotate given some definition of 3D blade shape. This is used as input to finite element (FE) computations to predict the forced response. The finite element results yield insight into how the blade shape can be altered to reduce unsteady stresses, and 3D single passage CFD enables quantification of the associated efficiency penalty.

The objectives of the work presented in this paper are, first, to describe and demonstrate an innovative analysis framework for computing unsteady rotor forces, intended for use in preliminary design. It enables assessment of the aerodynamically-induced unsteady blade loading and stresses caused by inlet flow distortion. A second objective is to quantify the trade-off between aerodynamic performance and unsteady blade stresses by considering two thickness distributions for a fan rotor with the same camber surface.

The key findings are that (1) the approach enables an estimation of loading vs. time for a rotor blade defined with any thickness distribution without recomputing the flow field,

(2) the nature of the non-uniform inflow tends not to alter the location of the highest time-varying stresses in the rotor blades, which is at the leading edge near the blade root, and (3) that both time-varying blade stress and stage isentropic efficiency are highly sensitive to changes in blade thickness distribution, even in low-speed flows.

For the example presented in the paper, thickening the rotor blade near the region of highest time-varying stress by at most 4% of chord locally leads to a decrease in design-point stage isentropic efficiency of 2.4% while the magnitude of the highest root-mean-squared (RMS) time-varying von Mises stress is decreased by a factor of 3.6.

The paper is organized as follows: First, the analysis approach is described conceptually and the numerical modelling approaches for the flow computations, 3D blade modelling, and determination of blade stresses are detailed. An example low-speed fan is also introduced. Second, the non-uniform flows studied are described and details of the resulting distortion-fan stage interactions are given. Subsequently the results of the FE analysis are presented and employed to guide a modification of the rotor blade thickness distribution which is shown to reduce unsteady stress at the cost of efficiency.

APPROACH

In this section, the conceptual analysis approach is described in detail, followed by the numerical modelling approaches for the flow computations, blade modelling, and FE analysis.

Unsteady Blade Loading Estimation

A body force model of the blade row(s) of interest is required. While the ideas that follow apply to any flow regime, without loss of generality we restrict our discussion to incompressible, inviscid flow and we use the analytical body force approach of Hall et al. [10] for a single-stage axial fan. The body force computed accounts only for loading and not viscous losses, so it acts perpendicularly to the relative streamlines. Further detail on this modelling approach is given in the following Section. The computation of the flow through a rotor would typically include an upstream duct, the fan rotor and stator, and a downstream duct to ensure the outlet boundary condition does not affect the flow in the blade rows. For some spatially non-uniform inflow, the flow and resultant body force field $\vec{F}_{\mathrm{bf}}$ in the rotor swept volume will in general be functions of the axial (x), radial (r), and circumferential (θ) location. As the body force represents a locally pitchwise-averaged effect of the blades on the flow, the local force per unit volume $\vec{F}_{\mathrm{blade}}$ (equal and opposite to $\vec{F}_{\mathrm{bf}}$) experienced by a blade at meridional location (x, r) within the rotor volume changes with time t:

$$\vec{F}_{\mathrm{blade}}(x, r, t) = -\vec{F}_{\mathrm{bf}}(x, r, \theta_0 + \Omega t). \tag{1}$$

where Ω is the rotor angular velocity. θ_0 is a function of x and r as defined by the blade camber surface (which must be known since it is required by the body force model). The

time resolution obtained is thus set by the number of circumferential grid points k in the body force computational grid: $\Delta t = 2\pi/(k\Omega)$. The local blade loading is obtained using Peters' method [11]. In Peters' approach, the local loading is computed using single-passage computations with the blades and the equivalent body force is computed. Here, we proceed in the opposite direction and use the computed body force to estimate the blade surface pressures. The vectors pointing from the camber surface to the suction side (SS) and pressure side (PS) of the blade are defined as

$$\hat{n}_{\mathrm{rf,PS}} = -\hat{n}_{\mathrm{rf,SS}} = \vec{F}_{\mathrm{bf}}/\left|\vec{F}_{\mathrm{bf}}\right| \tag{2}$$

so that these vectors act along the line of action of the body force and are thus perpendicular to the relative flow (rf) streamlines; the hat denotes unit magnitude. Given some blade thickness distribution, the blade surface intersections with these normals are the locations where the loading is defined. Note that, as implemented in this paper, this thickness distribution can be defined *after* the body force field has been computed. The local loading (pressure difference) is

$$\Delta p = \left|\vec{F}_{\mathrm{blade}}\right| \left(b \frac{2\pi r}{B} \frac{W_x}{W}\right) \tag{3}$$

where p is static pressure, B is the number of rotor blades, and b is the local fraction of open passage area

$$b = 1 - \frac{\Delta\theta_{\mathrm{blade}}}{2\pi/B} \tag{4}$$

with $\Delta\theta_{\mathrm{blade}} = q/r$ being the local blade thickness q divided by the local radius. W_x and $W = \left|\vec{W}\right|$ are the axial component and magnitude of the relative velocity, respectively. The factor in parentheses in Eq. 3 serves to 'smear out' the force per unit volume over a distance equivalent to the local blade pitch, minus the blade thickness, projected onto the line of action of $\vec{F}_{\mathrm{blade}}$. The pressure surface and suction surface pressures are computed by assuming that Δp is split equally:

$$p_{\mathrm{PS}} = p + \frac{1}{2}\Delta p$$
$$p_{\mathrm{SS}} = p - \frac{1}{2}\Delta p \tag{5}$$

This is the most significant simplifying assumption made in the modelling approach. The magnitude of the loading at any given point is not expected to be strongly affected by this assumption, however, since the rotor blades are in general thin compared to their chord.

These time-varying surface pressures can be applied as loading on a FE model of a rotor blade to ascertain the resulting time-varying stresses arising in response to the unsteady loading imposed by inlet distortion. The computational grid (nor, with the body force modelling approach used, the flow

field and body forces) is not dependent on the blade thickness distribution; as such, the distribution can be changed and the same $\vec{F}_{\text{blade}}$ field will produce a new set of p_{SS} and p_{PS} data. If a body force modelling approach which does use the blade thickness distribution is employed, the flow computations would need to be re-run if thickness is altered but the same grid could be used.

Body Force Model

The body force modelling approach of Hall et al. [10] is used to model the fan blade rows in this paper. With a body force model, computational cost is kept low because a steady, full-wheel computation is all that is required to capture the spatially-varying blade force associated with inlet distortion. The body force is defined:

$$\left|\vec{F}_{\text{bf}}\right| = 2\pi d \frac{\frac{1}{2}\rho W^2 / \left|\hat{n}_{\theta,\text{c}}\right|}{2\pi r / B} \tag{6}$$

where d is the deviation between the relative flow and the blade camber surface, ρ is the fluid density, and $\hat{n}_{\theta,\text{c}}$ is the tangential component of the blade camber surface unit normal vector. The direction of the body force is perpendicular to the relative velocity vector in the plane shared by the camber surface normal $\hat{n}_{\text{c}}$ and $\vec{W}$ such that it tends to drive the deviation towards zero. Since the model is only for normal (turning) forces and thus there are no viscous losses, Euler computations are used. It has been shown that distortion transfer is well-captured by this approach if the local rotor reduced frequency

$$f_{\text{red}} = \frac{c_x / V_x}{2\pi / \Omega} \tag{7}$$

is much less than one and if the longest length scale of the inlet distortions is much larger than one blade pitch [8, 10]. In Eq. 7 c_x is the blade axial chord, and V_x is the axial velocity. For the machine and distortions considered in this paper, $f_{\text{red}} < 0.1$ and the distortions have a maximum length scale $2\pi r$, which is 20 times larger than the blade pitch since there are $B = 20$ rotor blades.

ANSYS CFX 14 [12] is used to carry out the body force computations. CFX does not contain an Euler solver so laminar flow with zero-viscosity air and slip walls are used to simulate inviscid flow. The computational domain consists of the full annulus of the machine of interest including inlet and outlet ducts. Stagnation pressure and temperature along with flow direction are imposed at the inlet, while mass flow is specified at the outlet to yield the desired flow coefficient. Details regarding implementation for the specific fan studied are given later.

Blade Thickness Distribution and Single Passage Model

To determine the local loading Δp in Eq. 3, b and thus a blade thickness distribution is required. While any method

of generating a thickness distribution can be used, in this paper, the blade shapes are obtained using John Denton's open-source MULTALL turbomachinery design system [13]. Specifically, the 3D mesh generator Stagen 17.3 is used to define 3D models of the rotor and stator blades. Hub and casing curves, blade leading and trailing edge profiles, streamsurface camber lines along the span, and the maximum thickness on each streamsurface are provided as fixed inputs. The thickness distribution is defined by four additional parameters on each streamsurface: leading edge radius, trailing edge radius, location of maximum thickness, and a parameter defining the distribution of thickness. This latter parameter has extremes of constant thickness outside of the leading/trailing edge radii, and a linear increase from zero thickness at the leading edge to maximum thickness followed by a linear decrease towards zero thickness at the trailing edge. Stagen produces a fully structured H grid. A solid model of a rotor blade is constructed from the resulting mesh and this is used to compute b.

The MULTALL solver is employed to obtain single passage flow solutions including viscous effects to estimate the performance of the turbomachinery in uniform inflow at the flow coefficient of interest. This is most useful to (a) compare the performance of the body force model to the single passage model and (b) determine the changes in performance associated with altering the blade thickness distribution. At the inlet boundary condition, the stagnation pressure and temperature along with the flow direction are specified. Static pressure is specified at the outlet boundary and this is varied until the desired flow coefficient is obtained. A mixing plane is used between the rotor and stator as described by Denton [13].

Finite Element Analysis

The solid model of a rotor blade produced by Stagen is used to create a FE mesh for determining the time-varying stresses caused by inlet distortion. LSTC's LS-PrePost 4.5 [14] is used to create the FE mesh. In this paper a single rotor blade model is employed, with full boundary constraints prescribed to all nodes at the blade root. This assumes that the blade hub is infinitely rigid, but the approach could easily be expanded to include a full rotor with all blades and a hub to improve accuracy. A selective reduced integrated solid element formulation is implemented for all FE. In this paper, the blade is discretized with 3 elements through its thickness, 33 elements along the chord, and 50 elements along the span. Only one FE grid level is used since the aim of the paper is to illustrate the methodology, but grid independence could easily be assessed by generating a finer discretization.

Simulations are carried out using the FE solver LS-Dyna 9.2 [15]. The blade is set to be in solid body rotation about the fan axis; the rotational speed is increased from zero to the design speed smoothly (to ensure no discontinuities in angular acceleration) over the course of $\Delta t = 2/(2\pi\Omega_{\text{des}})$, the time period for two rotor revolutions at design speed (solid line in Fig. 1). The suction and pressure side time-varying pressure is obtained from the spatially-varying loading as described earlier and applied on the respective surface in the FE analysis. We assume steel blades with an elastic modulus of
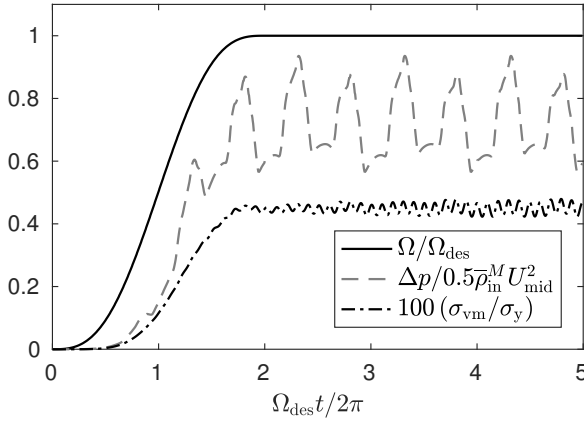
FIGURE 1. Angular velocity (solid black line), blade loading at mid-span and mid-chord (dashed grey line), and von Mises stress for central blade element at mid-span and mid-chord (black dashed-dotted line) vs. time for vertically-stratified inlet distortion with $\Delta p_t/\overline{\rho}_{in}^M U_{mid}^2 = 0.094$ and $\delta/2R_{in} = 0.50$.

207 GPa, Poisson's ratio of 0.3, and density of 7800 kg/m^3. Implicit time integration is utilized (time step size: 1000 steps per design-speed rotor revolution). Dynamic simulations are carried out. During the acceleration of the blade rotational speed, the time-varying loading also increases in amplitude (with the square of the rotational speed) and reaches 'full' amplitude when the blade rotational speed is at the design value. Subsequently the FE simulations are run for 3 more rotor revolutions. This is illustrated at mid-span and mid-chord by the dashed grey curve in Fig. 1 for one of the examples described later in the paper. The two peaks per revolution in the loading occur due to the way the loading is defined since $\hat{n}_{rf}$ is not perpendicular to the blade camber surface, but rather to the relative streamlines in the body force CFD; this results in phase shifts between pressure and suction side loading at a given (x, r) location. Also shown in the figure is the von Mises stress for the finite element at the centre of the blade (dashed-dotted black line). It is clear that higher frequencies dominate the stress response than the most energetic frequencies in the loading, and also that the time-varying portion of the stress is small compared to the time-averaged stress. Stress data from 3.5 to 4.5 revolutions is used for subsequent analyses.

Whittle Laboratory Low Speed Boundary-Layer-Ingesting Fan Rig

A specific turbomachine is required to demonstrate the approach. The fan geometry from the University of Cambridge Whittle Laboratory described in Refs. [16–18] is used for this purpose. Estimated blade row camber angle distributions are derived from radial distributions of leading and trailing edge metal angles assuming that the camber lines on streamsurfaces are circular arcs. Thickness distributions are estimated from radial distributions of maximum thickness-to-chord ratio. Table 1 contains key design parameters for the fan. All computations in this paper are carried out at the design point flow coefficient and corrected speed.

The stage geometry is modelled in both the body force

TABLE 1. Whittle Laboratory BLI fan rig design parameters

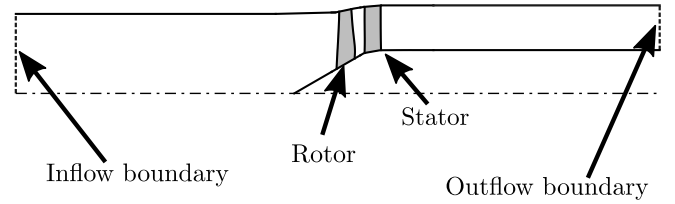|	
Flow coefficient, $\phi = \dot{m}/(\overline{\rho}_{in}^M A_{in} U_{mid})$	0.50
Stage work coefficient, $\psi = \Delta h_t/U_{mid}^2$	0.47
Stage pressure rise coefficient, $\Delta p_t/\overline{\rho}_{in}^M U_{mid}^2$	0.43
Stage reaction	0.81
Rotor corrected speed	1800 rpm
Rotor inlet tip Mach number	0.13
Rotor tip Reynolds number	2.0×10^5
Rotor inlet hub-to-tip radius ratio	0.3
Rotor inlet tip diameter	0.5 m
Number of rotor blades B	20
Number of stator vanes	30

FIGURE 2. Meridional view of body force computational domain, showing locations of blade rows and inflow/outflow boundaries.

CFD and in the single passage MULTALL computations. A meridional view of the computational domain used for the body force computations is depicted in Fig. 2. The grid contains 2.6×10^6 hexahedral cells and is fully structured. The grid is generated using Pointwise [19]. The body force approach reduces the grid size by a factor of approximately 30 compared to full-annulus bladed computations with boundary layers [17] and requires only a steady solution even in non-uniform inflow. As a result the computational cost is reduced by 2-3 orders of magnitude in addition to the detailed thickness distribution not being required to obtain the flow field. Four grid levels were created and the second of these was the coarsest which yielded grid-independent results. Subsequent refinement resulted in no further changes to the computed design work coefficient, which is $\psi = 0.485$. The work input is slightly over-predicted compared to the measured value in Table 1, but the agreement is good considering that the blade camber shape is estimated. The grid levels did not affect the characteristic slope. For the grid level selected, the rotor swept volume is resolved with 9 axial, 33 radial, and 256 circumferential cells.

A meridional view of the computational domain used for the single-passage MULTALL computations is shown in Fig. 3. The parameters chosen to define the blade thickness distribution are: leading edge radius of 1% of chord, trailing edge radius of 1% of chord, maximum thickness at 40% of chord, and the default thickness distribution parameter of 2.0. Three grids were generated using Stagen to ensure grid-independent results are obtained following the guidance in Ref. [13]. The selected grid is the second of the three levels with 54 pitch-wise grid points, 54 spanwise grid points, and 392 streamwise grid points. Additional refinement resulted in the stage
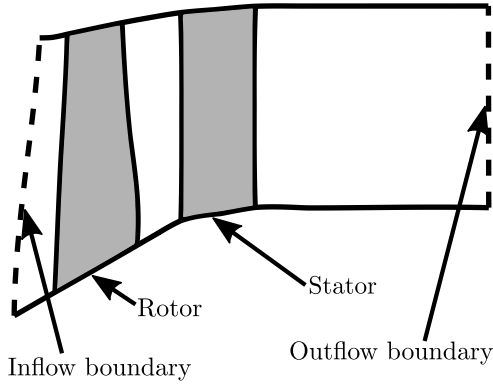
FIGURE 3. Meridional view of single-passage computational domain, showing locations of blade rows, and inflow/outflow boundaries.
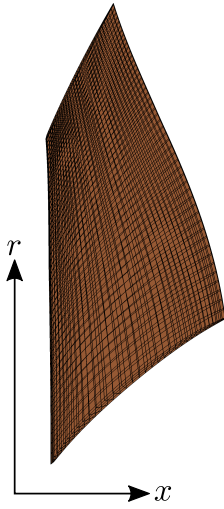

FIGURE 4. The finite element model of the Whittle fan rig rotor blade, viewed from the hub looking towards the tip.

pressure rise coefficient and isentropic efficiency changing by less than 0.1%. The design work coefficient computed using MULTALL is $\psi = 0.49$, in excellent agreement with the body force model. Further details of the computed aerodynamic performance are discussed later in the paper.

The finite element model of one rotor blade for the Whittle Laboratory BLI fan based on the geometry produced using Stagen is illustrated in Fig. 4.

INLET DISTORTIONS

In this paper six inlet distortions are considered. CFD flow fields using the body force model described earlier were available from the work reported in Defoe et al. [8]. The inlet distortions are divided into two types: vertically stratified and radially stratified.

The vertically stratified distortions have varying stagnation pressure which emulate those caused by boundary layer ingestion (BLI)-type propulsors integrated into an airframe. The intensity of the distortion is defined by a maximum stagnation pressure difference $\Delta p_t / \overline{\rho}_{\text{in}}^M U_{\text{mid}}^2$, where U_{mid} is the rotor speed at mid-span. The extent of the dis-

torted region is defined by the fraction of the inlet duct diameter over which the stagnation pressure varies, $\delta/2R_{\text{in}}$, where δ is the boundary layer thickness which yields the distortion and the inlet duct diameter is $2R_{\text{in}}$. Three distortions of this type are considered: $\Delta p_t / \overline{\rho}_{\text{in}}^M U_{\text{mid}}^2 = 0.094$ with $\delta/2R_{\text{in}} = 0.50$, $\Delta p_t / \overline{\rho}_{\text{in}}^M U_{\text{mid}}^2 = 0.117$ with $\delta/2R_{\text{in}} = 0.50$, and $\Delta p_t / \overline{\rho}_{\text{in}}^M U_{\text{mid}}^2 = 0.094$ with $\delta/2R_{\text{in}} = 1.00$.

The radially stratified distortions have varying stagnation pressure and stagnation enthalpy, and emulate the flow seen by the first compressor stage in a turboprop engine. In Ref. [8] these distortions could also include swirl, but here the inflow direction is always axial. In such a configuration the propeller is normally rotating about an axis offset from the engine core axis due to the gearbox between the core and propeller. The distortions are defined relative to the hypothetical rotation axis for an upstream isentropic propeller; primed quantities are defined relative to that axis. The non-dimensional gradient of the stagnation quantities is defined by

$$\frac{dh_t}{dr'} \frac{R_{\text{in}}}{U_{\text{mid}}^2} = \frac{dp_t}{dr'} \frac{R_{\text{in}}}{\overline{\rho}_{\text{in}}^M U_{\text{mid}}^2}. \tag{8}$$

The equality is the result of assuming that the propeller is isentropic and the Mach numbers are everywhere small. In Eq. 8, h_t is the stagnation enthalpy and p_t is the stagnation pressure. The offset between fan and propeller axes, normalized by duct inlet radius, is $\Delta R/R_{\text{in}}$. Three distortions of this type are considered in this paper: $\frac{dh_t}{dr'} \frac{R_{\text{in}}}{U_{\text{mid}}^2} = 1.85$ with $\Delta R/R_{\text{in}} = 0.25$, $\frac{dh_t}{dr'} \frac{R_{\text{in}}}{U_{\text{mid}}^2} = 1.85$ with $\Delta R/R_{\text{in}} = 0.75$, and $\frac{dh_t}{dr'} \frac{R_{\text{in}}}{U_{\text{mid}}^2} = 2.81$ with $\Delta R/R_{\text{in}} = 0.75$. Note that as described by Defoe et al. [8], for these magnitudes of distortion in low-speed flow it is the variation in stagnation pressure which dominates the rotor distortion response.

Due to the fact that fan and compressor rotors in general attenuate stagnation pressure distortions, the circumferential non-uniformities are the largest near the rotor leading edge. Figure 5 shows the rotor leading edge static pressure field and body force per unit volume for the three vertically stratified distortions, while Fig. 6 shows the same quantities for the three radially stratified distortions. As can be seen, the fundamental period of all the distortions is once per revolution. The static pressure distortions are largest at the hub. Due to the different nature of the distortions, the radially stratified distortions yield more complex body force distributions than do the vertically stratified distortions. Further discussion as to the physical mechanisms responsible for the behaviour observed can be found in Ref. [8].

FAN AERODYNAMIC PERFORMANCE AND TIME-VARYING STRESS

In this section, the approach described earlier is applied for the six inlet distortions studied. The resulting aerodynamic performance and time-varying rotor blade stress for the fan is presented. The modal nature of the response is not assessed, being beyond the scope of this paper, but the FE
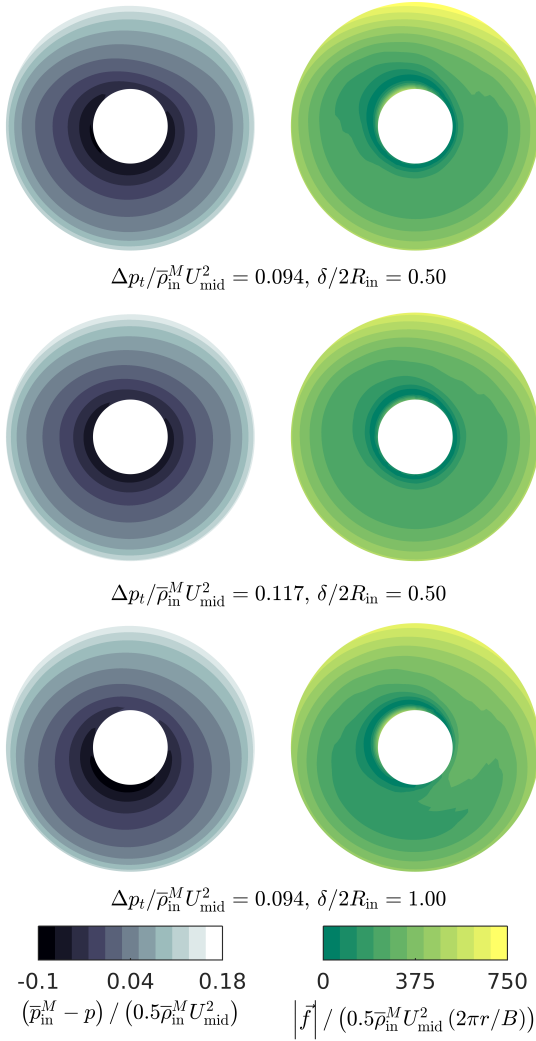
FIGURE 5. Computed rotor leading edge static pressure distribution (left) and body force per unit volume (right) for vertically stratified distortions. Top: $\Delta p_t/\overline{\rho}_{\mathrm{in}}^M U_{\mathrm{mid}}^2 = 0.094$ with $\delta/2R_{\mathrm{in}} = 0.50$; centre: $\Delta p_t/\overline{\rho}_{\mathrm{in}}^M U_{\mathrm{mid}}^2 = 0.117$ with $\delta/2R_{\mathrm{in}} = 0.50$; bottom: $\Delta p_t/\overline{\rho}_{\mathrm{in}}^M U_{\mathrm{mid}}^2 = 0.094$ with $\delta/2R_{\mathrm{in}} = 1.00$.
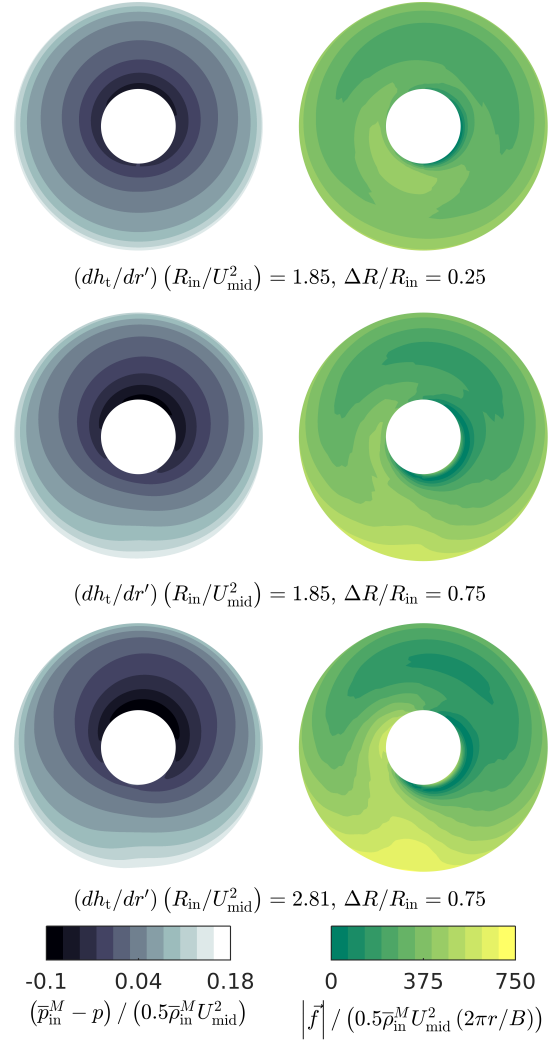
FIGURE 6. Computed rotor leading edge static pressure distribution (left) and body force per unit volume (right) for radially stratified distortions. Top: $\frac{dh_t}{dr'}\frac{R_{\mathrm{in}}}{U_{\mathrm{mid}}^2} = 1.85$ with $\Delta R/R_{\mathrm{in}} = 0.25$; centre: $\frac{dh_t}{dr'}\frac{R_{\mathrm{in}}}{U_{\mathrm{mid}}^2} = 1.85$ with $\Delta R/R_{\mathrm{in}} = 0.75$; bottom: $\frac{dh_t}{dr'}\frac{R_{\mathrm{in}}}{U_{\mathrm{mid}}^2} = 2.81$ with $\Delta R/R_{\mathrm{in}} = 0.75$.

results obtained would permit an investigation of the modal excitations incurred by the inlet distortions.

First, the results for the initial rotor blade thickness distribution are discussed. An analysis of the stress distribution leads to a suggested change in thickness distribution. The subsequent changes in performance and stress are then quantified.

Baseline Thickness Distribution

Fan Aerodynamics The fan aerodynamic performance in uniform flow at the design flow coefficient is computed using MULTALL. As stated earlier the work coefficient is found to be $\psi = 0.49$. The pressure rise coefficient $\Delta p_t/\overline{\rho}_{\mathrm{in}}^M U_{\mathrm{mid}}^2 = 0.44$ for the rotor and 0.43 for the stage yielding a rotor isentropic efficiency of 91.3% and a stage isentropic efficiency of 89.1%. The efficiency in non-uniform flow is typically lower by 1-2% [9, 17, 20]. Here we assume that efficiency *changes* associated with alterations to the blade thickness distribution are the same in uniform and non-uniform inflow. Particularly for the low-speed fan considered, this is a reasonable assumption since the upstream influence of the rotor tends to preclude extremely large swings in incidence at the rotor leading edge.

Time-Varying Rotor Blade Stress The metric used to assess the blade stresses is the von Mises stress σ_{vm}. This is normalized by the blade material yield stress, taken to be $\sigma_y = 350$ MPa. Over one rotor revolution, the focus is on the time-varying von Mises stress since the overall stress level is small: it never exceeds 14% of the yield stress. This
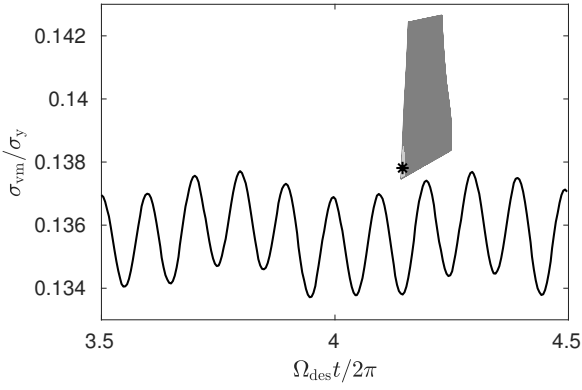
7

FIGURE 7. Normalized von Mises stress vs. time for element with highest time-varying RMS stress. Vertically stratified distortion with $\Delta p_t / \overline{\rho}_{\mathrm{in}}^M U_{\mathrm{mid}}^2 = 0.094$ and $\delta/2R_{\mathrm{in}} = 0.50$. Inset: meridional view of rotor blade showing locations of elements in 99th percentile of RMS time-varying von Mises stress (light grey). Location of element with highest time-varying RMS stress highlighted (star).

is due to the low-speed flow considered. To quantify the time-varying stress, the RMS time-varying von Mises stress $\sigma_{\mathrm{vm,RMS}}$ is used:

$$\sigma_{\mathrm{vm,RMS}} = \sqrt{\frac{\Omega_{\mathrm{des}}}{2\pi} \int_{t_0}^{t_0 + 2\pi/\Omega_{\mathrm{des}}} (\sigma_{\mathrm{vm}} - \overline{\sigma}_{\mathrm{vm}})^2 \, dt} \qquad (9)$$

where $\overline{\sigma}_{\mathrm{vm}}$ is the time-average von Mises stress:

$$\overline{\sigma}_{\mathrm{vm}} = \frac{\Omega_{\mathrm{des}}}{2\pi} \int_{t_0}^{t_0 + 2\pi/\Omega_{\mathrm{des}}} \sigma_{\mathrm{vm}} dt. \qquad (10)$$

For blades with much higher loading, it would be more appropriate to use fatigue life criteria instead of the RMS time-varying von Mises stress.

The region of the blade with the highest $\sigma_{\mathrm{vm,RMS}}$ is around the leading edge near the hub for all six inlet distortions considered. This is not unexpected since, as discussed earlier and shown in Figs. 5 and 6, the flow and thus loading non-uniformity is highest near the leading edge at the hub. In addition, the rotation of the fan increases stress at lower radii. Figure 7 depicts the von Mises stress for the element with the highest $\sigma_{\mathrm{vm,RMS}}$ ($\sigma_{\mathrm{vm,RMS}}/\sigma_y = 1.17 \times 10^{-3}$) for the worst case (vertically stratified distortion with $\Delta p_t / \overline{\rho}_{\mathrm{in}}^M U_{\mathrm{mid}}^2 = 0.094$ and $\delta/2R_{\mathrm{in}} = 0.50$); the inset shows the meridional locations of the elements in the 99th percentile of $\sigma_{\mathrm{vm,RMS}}$. The element for which the stress vs. time is shown is highlighted.

Returning to the observation made earlier that higher frequencies dominate the stress response than the most energetic loading frequencies, frequency spectra for both the pressure side loading applied adjacent to the element with the highest $\sigma_{\mathrm{vm,RMS}}$ as well as σ_{vm} for that element are plotted together
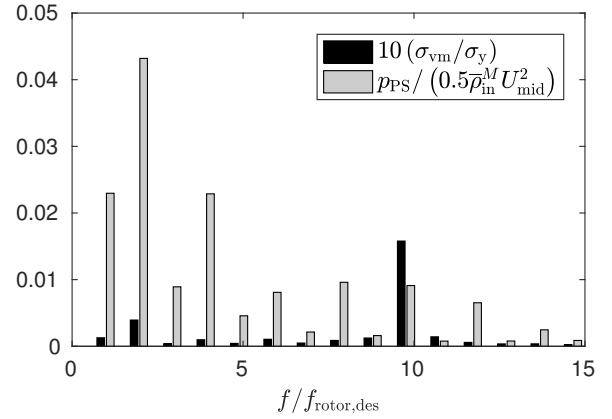

FIGURE 8. Frequency spectra of pressure side loading and von Mises stress for the element highlighted in Fig. 7. Vertically stratified distortion with $\Delta p_t / \overline{\rho}_{\mathrm{in}}^M U_{\mathrm{mid}}^2 = 0.094$ and $\delta/2R_{\mathrm{in}} = 0.50$. $f = 0$ components not shown for clarity.

in Fig. 8. The zero-frequency component is not shown because it is much larger than the harmonics. It can be seen that while the first, second, and fourth harmonics dominate the frequency spectrum of the loading, the 10th harmonic dominates the stress response. This is likely due to excitation of a natural frequency of the blade.
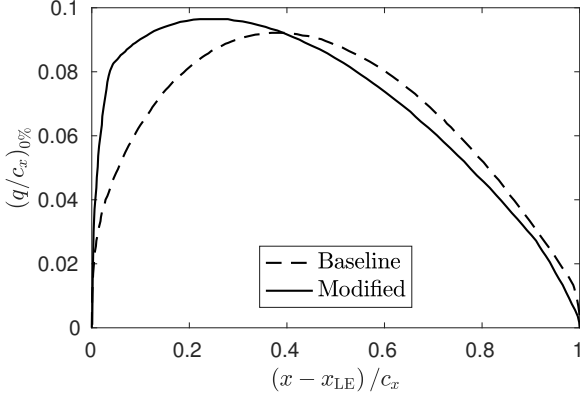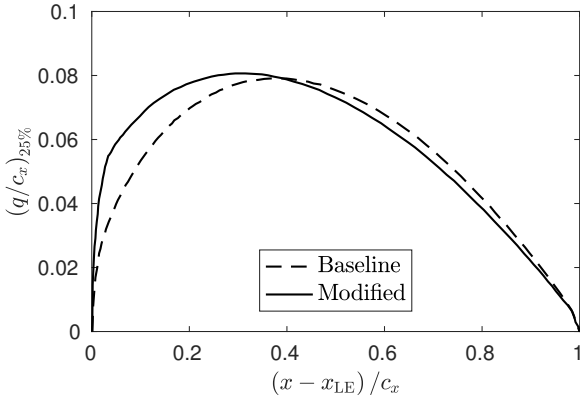
Modified Thickness Distribution

To provide a quantification of the trade-off between $\sigma_{\mathrm{vm,RMS}}$ and aerodynamic efficiency, we modify the blade thickness distribution based on the region of highest $\sigma_{\mathrm{vm,RMS}}$ identified for the initial, baseline thickness distribution (leading edge, first $\sim 25\%$ span). The specific changes are tabulated in Table 2. The blade is defined in Stagen by sections at the hub, 25% span, 50% span, 75% span, and tip. Only sections at the hub and 25% are modified; no changes are made to sections at or above 50% span. The blade shape is interpolated between section definitions, so some modification occurs up to just below 50% span. The resulting thickness distributions at the hub and at 25% span are shown in Figs. 9 and 10, respectively. The largest increase in thickness is at the hub near 5% chord, where an additional 4% chord of thickness is added. The net effect of the changes is seen to be to shift the thicker portion of the blade forward while slightly increasing maximum thickness.

Fan Aerodynamic Performance Comparison

The increased thickness near the hub decreases overall rotor and stage performance as computed at the design flow coefficient using MULTALL. The work coefficient is unchanged at 0.49. Table 3 lists performance metrics for the rotor and stage for the two thickness distributions. With the thicker rotor blade, the rotor efficiency falls by 2.2% while stage efficiency drops by 2.4%. The additional losses giving rise to the reduced efficiency are concentrated in the inner 60% of span as shown in Fig. 11, which is a plot of the spanwise distribution of entropy-based loss coefficient across the rotor ω_{rot} for the two thickness distributions. The reason for the increased loss is elucidated in Fig. 12, which depicts entropy
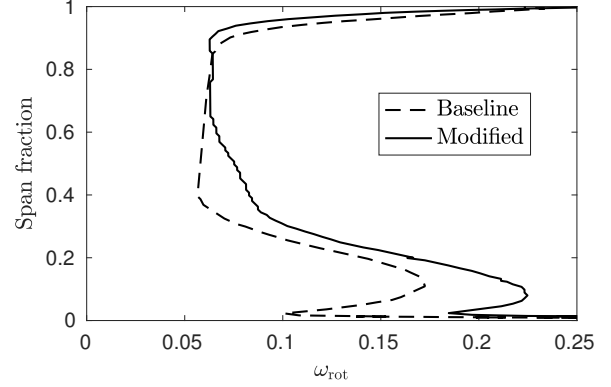
TABLE 2. Fan blade thickness distribution details: baseline and modified.

Quantity	Baseline	Modified
Hub leading edge radius, $(R_{LE}/c_x)_{0\%}$	0.010	0.035
25% span leading edge radius, $(R_{LE}/c_x)_{25\%}$	0.010	0.023
Hub maximum thickness, $(q/c_x)_{0\%}$	0.092	0.096
25% span maximum thickness, $(q/c_x)_{25\%}$	0.079	0.081
Location of maximum thickness at hub, $(x_{q,\max}/c_x)_{0\%}$	0.40	0.25
Location of maximum thickness at 25% span, $(x_{q,\max}/c_x)_{25\%}$	0.40	0.29

FIGURE 9. Rotor blade thickness distributions at the hub.

FIGURE 10. Rotor blade thickness distributions at 25% span.

TABLE 3. Fan rotor and stage performance comparison: baseline vs. modified blade thickness distribution.

Quantity	Baseline	Modified
Rotor pressure rise coefficient	0.44	0.43
Stage pressure rise coefficient	0.43	0.42
Rotor isentropic efficiency	91.3%	89.1%
Stage isentropic efficiency	89.1%	86.7%

function $\exp(-\Delta s/\mathscr{R})$ at 12.5% span through the rotor blade passage for the baseline and modified rotor blades (halfway between the two modified sections). Lower values correspond to increased entropy and thus higher loss. Though the losses associated with the blade boundary layers are similar for both blade sections, the thicker blade increases velocities in the passage, driving higher mid-passage losses that arise from the hub boundary layer and secondary flows.

FIGURE 11. Spanwise distribution of rotor exit entropy-based loss coefficient ω_{rot} for baseline and modified blade thickness distributions.

Time-Varying Rotor Blade Stress Comparison

For the modified blade, a finite element mesh is created in exactly the same way as for the baseline blade. From this the surface pressure loading is determined so that FE simulations can be carried out for all six inlet distortions as was done for the baseline blade. It is found that in general the blade region with the highest $\sigma_{vm,RMS}$ is again the same for all six distortions, though they are distributed higher up the span near the leading edge than for the baseline blade. Figure 13 depicts the time-varying von Mises stress for the element with the highest $\sigma_{vm,RMS}$ for the worst case with the modified blade (radially stratified distortion with $\frac{dh_t}{dr'}\frac{R_{in}}{U_{mid}^2} = 2.81$ and $\Delta R/R_{in} = 0.75$) as well as the same data plotted in Fig. 7 (baseline thickness, $\Delta p_t/\overline{\rho}_{in}^M U_{mid}^2 = 0.094$ and $\delta/2R_{in} = 0.50$); the inset shows the meridional locations of the element with the highest $\sigma_{vm,RMS}$ for each case. Recall that with the baseline blade the maximum $\sigma_{vm,RMS}/\sigma_y = 1.17 \times 10^{-3}$ while for the modified blade we obtain maximum $\sigma_{vm,RMS}/\sigma_y = 3.27 \times 10^{-4}$, a reduction by a factor of 3.6, due entirely to the thickening of the rotor blade near the hub leading edge.

This brief analysis quantifies the trade-off between aerodynamic efficiency and time-varying stress reduction: 2.4% stage efficiency reduction in exchange for reducing $\sigma_{vm,RMS}$ to less than one-third of its baseline value. In this case, due to the low magnitude of the time-varying stress, thickening blade sections would likely not be required. However a similar fan design intended for operation in flows at higher velocities would see stresses scale roughly with rotational speed squared (assuming constant flow coefficient). This is because pressure differences scale with velocity squared. Thus,
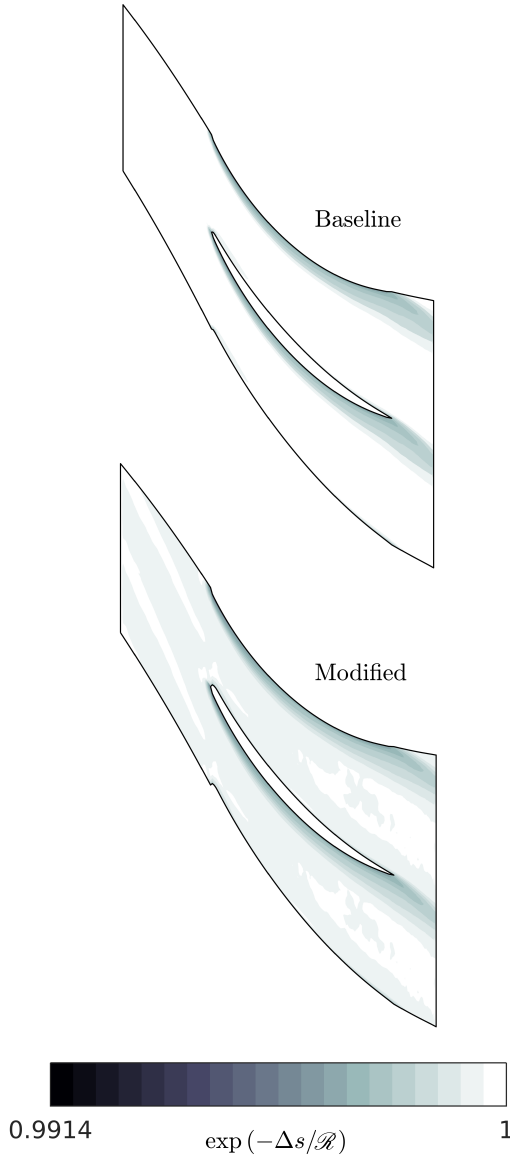
FIGURE 12. Computed entropy function at 12.5% span in the rotor. Top: baseline rotor blade. Bottom: modified rotor blade.

in higher speed flows, quantifying the trading relationship between efficiency and time-varying stress/fatigue life (as controlled by blade thickness distribution) becomes an important part of blade design for applications in which continuous operation with inlet distortion is required (for example, BLI propulsors).

SUMMARY AND CONCLUSIONS

In this paper, an approach for estimating unsteady rotor loading caused by inlet distortion was presented and demonstrated. The key feature of the approach is that the full-annulus flow field is computed using a body force model of the turbomachinery. The body force model used does not require that a blade thickness distribution be specified; only the blade camber surface is required. Given a subsequently defined rotor blade thickness distribution, the surface pressures are determined as a function of time and single passage
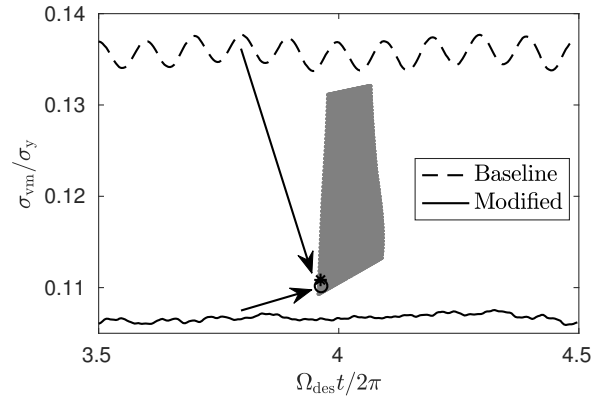

FIGURE 13. Normalized von Mises stress vs. time for elements with highest RMS time-varying stress for (dashed line) vertically stratified distortion with $\Delta p_t / \overline{p}_{in}^M U_{mid}^2 = 0.094$ and $\delta / 2R_{in} = 0.50$ with baseline thickness and for (solid line) radially stratified distortion with $\frac{dh_t}{dr'} \frac{R_{in}}{U_{mid}^2} = 2.81$ and $\Delta R / R_{in} = 0.75$ with modified thickness. Inset: locations of element with highest RMS time-varying von Mises stress for each case (star: baseline; circle: modified).

CFD is used to determine stage performance. The surface pressures are the loading inputs to a FE simulation which yields the time-varying stress in the rotor blades. In this paper CFX was used for the body force CFD, Stagen was used to generate the blade profiles, MULTALL was used to compute the single passage flow fields, and LS-Dyna was used for the FE analysis. The approach is intended for use at the preliminary design stage for applications where a fan or compressor is required to operate continuously with inlet distortion.

The utility of the approach was demonstrated through its application to a low-speed fan. For this fan and six inlet distortions studied, it was found that thickening the rotor blades near the leading edge in the inner half of the span was able to reduce the maximum RMS time-varying stress by a factor of 3.6. The associated penalty to efficiency was 2.2% for the rotor and 2.4% for the stage.

For the fan studied, the key findings are that (1) the blade root near the leading edge is the region with the highest time-varying stress regardless of the details of the inlet distortion, (2) low-amplitude, high-frequency components of the time-varying blade surface loading can excite the largest excitations in the blade stress response, and (3) increasing blade thickness in the regions of high time-varying stress significantly reduces aerodynamic efficiency but yields proportionally much larger reductions in time-varying stress.

In this paper the RMS time-varying von Mises stress, $\sigma_{vm,RMS}$, was used as a metric for assessing the impact of inlet distortion on the rotor blades. A more useful metric for high-speed machines would be an estimate of the blade fatigue life, but since the example fan studied is a low-speed machine fatigue life is not a concern.

To avoid having to recompute the the body force CFD solutions, the rotor and stator camber surfaces were constrained to remaind constant. As a result, even when the blade thickness distribution was altered, the work coefficient (0.49) was not altered. However, this meant that the lower efficiency associated with thicker rotor blades resulted in reduced pres-

sure rise. In practice the required pressure rise is likely to be a hard constraint and the rotor blade camber would need to be altered along with thickness to increase work input so as to maintain the design intent pressure rise. Since increasing camber at constant incidence tends to increase loss, the increase in blade camber required to achieve the design intent pressure rise might be significant when blade sections are thickened. This would necessitate new body force CFD flow solutions. In that case the approach could be used as part of a coupled optimization scheme which combines body force CFD, single-passage CFD for determining efficiency, and FE analysis to determine stress. Such an optimization approach could yield designs which ensure high rotor efficiency for a required pressure rise and mass flow subject to constraints on maximum allowable time-varying stress (or minimum required fatigue life).

An additional limitation of the approach is that the coupling between the aerodynamics and aeromechanics is one-way: the fluid flow influences the blade stresses and strains but the reverse is not true. This is acceptable so long as blade deflections remain small, but in the case of blade flutter two-way coupling is required and the current approach would be unsuitable.

Future work should compare the loading and stresses produced by the approach described in this paper to existing higher-fidelity methods to quantify its accuracy.

ACKNOWLEDGMENT

REFERENCES

[1] He, L., 2010. "Fourier Methods for Turbomachinery Applications". *Prog. in Aerospace Sci., 46*(8), pp. 329–341.

[2] Hall, K. C., Thomas, J. P, and Clark, W. S., 2002. "Computation of Unsteady Nonlinear Flows in Cascades Using a Harmonic Balance Technique". *AIAA Journal, 40*(5), pp. 879–886.

[3] Rahmati, M. T., He, L., Wang, D. X., Li, Y. S., Wells, R. G., and Krishnababu, S. K., 2013. "Nonlinear Time and Frequency Domain Methods for Multirow Aeromechanical Analysis". *J. Turbomach., 136*(4), p. 041010.

[4] Manwaring, S. R., Rabe, D. C., Lorence C. B., and Wadia, A. R., 1997. "Structures and Dynamics Committee Best Paper of 1996 Award: Inlet Distortion Generated Forced Response of a Low-Aspect-Ratio Transonic Fan". *J. Turbomach., 119*(4), pp. 665–676.

[5] Marble, F., 1964. *Three-Dimensional Flow in Turbomachines*, Vol. 10 of *High Speed Aerodynamics and Jet Propulsion*. Princeton University Press, pp. 83–166.

[6] Horlock, J. H. and Marsh, H., 1971. "Flow Models for Turbomachines". *Journal of Mechanical Engineering Science, 13*(5), pp. 358–368.

[7] Horlock, J. H., 1971. "On Entropy Production in Adiabatic Flow in Turbomachines". *Journal of Fluids Engineering, 93*(4), pp. 587–593.

[8] Defoe, J. J., Etemadi, M., and Hall, D. K., 2018. "Fan Performance Scaling with Inlet Distortions". *J. Turbomach., 140*(7), p. 071009.

[9] Hill, D. J. and Defoe, J. J., 2018. "Innovations in Body Force Modeling of Transonic Compressor Blade Rows". *International Journal of Rotating Machinery, 2018*, p. 6398501.

[10] Hall, D. K., Greitzer, E. M., and Tan, C. S., 2017. "Analysis of Fan Stage Conceptual Design Attributes for Boundary Layer Ingestion". *J. Turbomach., 139*(7), March, p. 071012.

[11] Peters, A., 2014. "Ultra-Short Nacelles for Low Fan Pressure Ratio Propulsors". PhD thesis, MIT, Department of Aeronautics and Astronautics, February.

[12] ANSYS, Inc., 2011. ANSYS® CFX, Release 16.2, ANSYS CFX-Solver Theory Guide.

[13] Denton, J. D., 2017. "Multall - An Open Source, Computational Fluid Dynamics Based, Turbomachinery Design System". *J. Turbomach., 139*(12), p. 121001.

[14] Livermore Software Technology Corporation, 2012. LS-PrePost Online Documentation, http://www.lstc.com/lspp/.

[15] Hallquist, J. O., 2006. LS-DYNA Theory Manual Version. Livermore Software Technology Corporation.

[16] Gunn, E. J., Tooze, S. E., Hall, C. A., and Colin, Y., 2013. "An Experimental Study of Loss Sources in a Fan Operating with Continuous Inlet Stagnation Pressure Distortion". *J. Turbomach., 135*(5), p. 051002.

[17] Gunn, E. J. and Hall, C. A., 2014. "Aerodynamics of Boundary Layer Ingesting Fans". In Proceedings of ASME Turbo Expo 2014: Turbine Technical Conference and Exposition, ASME. Paper number GT2014-26142.

[18] Perovic, D., Hall, C. A., and Gunn, E. J., 2015. "Stall Inception in a Boundary Layer Ingesting Fan". In Proceedings of ASME Turbo Expo 2015: Turbine Technical Conference and Exposition, ASME. Paper number GT2015-43025.

[19] Pointwise, Inc., 2018. Pointwise® User Manual.

[20] Fidalgo, V. J., Hall, C. A., and Colin, Y., 2012. "A Study of Fan-Distortion Interaction Within the NASA Rotor 67 Transonic Stage". *J. Turbomach., 134*(5), p. 051011.

---

[1]www.sharcnet.ca